Nuclear Instruments and Methods in Physics Research A 653 (2011) 176–180

Contents lists available at ScienceDirect

Nuclear Instruments and Methods in Physics Research A

journal homepage: www.elsevier.com/locate/nima

Experimental study of fast electron propagation in compressed matter

B. Vauzour [a], J.J. Santos [a,*], D. Batani [c], S.D. Baton [b], M. Koenig [b], Ph. Nicolaï [a], F. Perez [b], F.N. Beg [d], C. Benedetti [e], R. Benocci [c], E. Brambrink [b], S. Chawla [d], M. Coury [f], F. Dorchies [a], C. Fourment [a], M. Galimberti [h], L.A. Gizzi [i], R. Heathcote [h], D.P. Higginson [d], J.J. Honrubia [g], S. Hulin [a], R. Jafer [c], L.C. Jarrot [d], L. Labate [i], K. Lancaster [h], P. Köster [i], A.J. MacKinnon [j], P. McKenna [f], A.G. McPhee [j], W. Nazarov [k], J. Pasley [l], R. Ramis [g], Y. Rhee [m], C. Regan [a], X. Ribeyre [a], M. Richetta [n], F. Serres [b], H.-P. Schlenvoigt [b], G. Schurtz [a], A. Sgattoni [e], C. Spindloe [h], X. Vaisseau [a], L. Volpe [c], V. Yahia [b]

[a] Université de Bordeaux – CNRS – CEA, Centre Lasers Intenses et Applications (CELIA), Talence, France
[b] Laboratoire pour l'Utilisation des Lasers Intenses, UMR 7605 CNRS-CEA-Ecole Polytechnique-Univ. Paris VI, Palaiseau, France
[c] Dipartimento di Fisica, Università di Milano-Bicocca, Milano, Italy
[d] University of California, San Diego, La Jolla, USA
[e] Dipartimento di Fisica, Università di Bologna, Bologna, Italy
[f] SUPA, Department of Physics, University of Strathclyde, Glasgow, UK
[g] ETSI Aeronauticos, Universidad Politécnica de Madrid, Madrid, Spain
[h] Central Laser Facility, Rutherford Appleton Laboratory, Didcot, UK
[i] Intense Laser Irradiation Laboratory at INO-CNR, Pisa, Italy
[j] Lawrence Livermore National Laboratory, Livermore, USA
[k] University of St Andrews, UK
[l] Department of Physics, University of York, York, UK
[m] KAERI, Republic of Korea
[n] Dipartimento di Ingegneria Meccanica, Università di Roma Tor Vergata, Roma, Italy

ARTICLE INFO

Available online 21 December 2010

Keywords:
Compression
Electron transport
Fast Ignition
X-ray radiography
Proton radiography
Hydrodynamic simulations

ABSTRACT

We report on experimental results of the fast electron transport in compressed plasmas, created by laser-induced shock propagation in both cylindrical and planar geometry. Two experiments were carried out. The first one was based on the compression of a polyimide cylinder filled with foams of three different initial densities (ρ_0). X-ray and proton radiographies of the target during the compression coupled with hydrodynamic simulations show that the obtained core densities and temperatures range from 2 to 11 g/cm^3 and from 30 to 120 eV, respectively. By studying the K-shell fluorescence from dopant atoms inside the target and from tracer layers situated at both front and rear side of the target it has been possible to investigate the fast electron propagation. The results show that Cu K_α yield emitted by the target rear side foil decreases with increasing compression, independently of ρ_0. An electron collimation can also be observed for certain experimental conditions where a convergent resistivity gradient interacts with the fast electron beam. The second experiment was performed in a planar geometry with a compressing shock counter-propagative to the fast electron beam. In this case the areal density ρz seen by the electrons is constant during the compression in such a way that changes in the fast electron range should be ascribed to collective mechanisms. The study of the K_α fluorescence, from buried fluorescent layers of different atomic numbers, shows that the electrons with energy <75 keV are more affected by resistive losses in compressed compared to non-compressed targets. These two experiments were part of the Experimental Fusion Validation Program of the HiPER project.

1. Introduction

In the Fast Ignition (FI) scheme [1] of the Inertial Confinement Fusion (ICF), a small sphere of CH filled with a Deuterium–Tritium (D–T) mixture is compressed by multi 100 kJ laser beams. At stagnation a relativistic electron current, generated by short pulse high intensity laser beams, propagates in the compressed region over approximately 100 μm from the critical density region ($\rho \sim 1-10$ g/cm^3, $T \sim 1-10$ eV) till the compressed core ($\rho \sim 400$ g/cm^3 and $T \sim 300$ eV) where it efficiently deposits the main part of its energy (15–20 kJ in less than 20 ps) and thus heats the fuel to thermonuclear fusion ignition conditions. Crucial issues

* Corresponding author.
E-mail address: Santos.Joao@celia.u-bordeaux1.fr (J.J. Santos).

0168-9002/$ - see front matter © 2010 Elsevier B.V. All rights reserved.
doi:10.1016/j.nima.2010.12.062

of this ignition scheme remain in the control of the fast electron source and its transport through a highly overdense plasma. Several experiments have been realized using cold solid targets in planar geometry in order to investigate the laser to fast electron energy coupling efficiency [2], the fast electron beam divergence [3,4] or temperature [5]. However, in such experiments the achieved plasma densities and temperatures are far from those expected in the case of FI. Such difference could exhibit a modified behavior in the fast electron population especially in the electron stopping power or their divergence.

The two experiments described hereafter were designed to study the transport of fast electrons in compressed targets. The first experiment [6] (Section 2) consisted to radially compress a hollow cylindrical target filled with foams at different initial densities ρ_0 and to study the fast electron transport along the cylinder axis. This compression geometry allows to achieve higher temperatures and compression factors than obtained in a simple planar compression, approaching plasma conditions of the dense region around the compressed D–T in an imploded FI target [7]. Nonetheless, in this case, the compressed region radius is limited to few tens of microns. The second experiment (Section 3) was devoted to the electron transport in 1D-counter-propagative shock compressed target (i.e. the electrons propagate in the opposite direction to the shock). During the compression the areal density seen by the electron beam is constant. As the collisional energy losses depend mostly on the areal density, a modified behavior in the fast electron transport between compressed and non-compressed targets should be essentially ascribed to collective mechanisms.

2. Cylindrical compression experiment

2.1. Experimental setup

The experiment has been performed on the VULCAN TAW laser facility at RAL (UK). Four long pulses (LP) high intensity laser beams (4×70 J, 1 ns, 0.53 μm at 2ω) were used to radially compress 200 μm long, 220 μm outer diameter and 20 μm thick polyimide cylinders ($\rho_{poly}=1.1$ g/cm^3) filled with CH foams of three different initial densities ($\rho_0=0.1$, 0.3 or 1 g/cm^3). The cylinders were closed by 20 μm Ni and Cu foils placed, respectively, at the front and at the rear side. An additional short pulse (SP) beam (5×10^{18} W cm^{-2}, 10 ps at ω) was focused on the Ni foil to generate a fast electron current at the front side of the cylinder. In order to prevent the interaction of the SP beam with low density ablation plasma created by the LP beams during the compression, a tube-shaped plastic coated gold shield was stuck onto the Ni foil (see Fig. 1). The target design was previously optimized using the 2D-hydrodynamic code CHIC [8] developed at CELIA, according to the VULCAN laser specifications to produce classic, coupled and coupled and degenerated plasmas for, respectively, $\rho_0=0.1$, 0.3 or 1 g/cm^3.

The fast electron current was generated at various times during the compression by introducing a delay ($0\le\tau\le3.5$ ns) between the SP and the LP beams with an accuracy of ±100 ns (due to the jitter).

The experiment was split into two phases. The first phase was devoted to the characterization of the plasma parameters (density and temperature) of the cylinder at different stages of the compression. In this phase the fast electron current was not generated and the SP beam was focused on a 25 μm thick Ti foil to produce an X-ray backlight source for X-ray radiography diagnostic [9]. The X-ray source, placed 10 mm aside to the target, probed the cylinder transversally at different delays τ during the compression. A spherical quartz crystal ($2d=2.748$ Å, $R_c=380$ mm with d the inter-reticular distance and R_c the radius of curvature) was located 200 mm across the target and imaged the cylinder onto an imaging plate placed 2 m away. We slightly rotated the crystal to 0.5° so that it only reflected the 4.5 keV Ti K_α radiation according to Bragg's law. The total magnification of the system was estimated to $M=10.7$ with a spatial resolution $\Delta x\sim20$ μm in the target plane. In order to improve the contrast ratio of the X-ray radiography, 30% (in mass) of Cl atoms were mixed with the CH foam (for this phase only). A transverse point projection proton radiography [10] diagnostic was also implemented to study the compression of 0.1 g/cm^3 targets. However, in this paper we focus only on the X-ray radiography. For more information about proton radiography refer to Ref. [11].

The second phase was dedicated to the study of the fast electron propagation inside the compressed cylinder. This study was monitored by the K-shell fluorescence emitted by Ni and Cu foils, respectively, at the front and rear side of the cylinder. In order to observe the electrons propagation between these two foils the CH foam was doped with 20% (in mass) of Cu atoms (only 10% for 1 g/cm^3 targets). Two spherically bent quartz crystals ($2d=1.541$ Å, $R_c=380$ mm) were used to image the Cu K_α (8.05 keV) fluorescence produced by the electrons propagation. The two crystals were placed to simultaneously detect side on and rear-view images of the Cu K_α emission. Two X-ray spectrometers were also implemented. The first one, based on a cylindrical quartz crystal ($2d=1.012$ Å, $R_c=100$ mm) in Von-Hamos configuration, produced time- and space-integrated spectra of the X-ray emission in the 7.3−9.3 keV range including both Ni and Cu K-shell fluorescence lines, with a spectral resolution of 3 ± 2 eV. The second one, which monitored the same spectral range, was made of a planar highly oriented pyrolitic graphite crystal (HOPG). In this second case the resolution was lower (around 50 eV), but the signal-to-noise ratio was better.

2.2. Results and interpretation

In Fig. 2b is presented a typical X-ray radiography obtained during the compression of the cylinder. For comparison we show a photography of the same target before the laser shot (Fig. 2a).

The experimental diameter ("Full Width at Half Maximum": *FWHM*) of the cylinder is measured at different times, to reconstruct

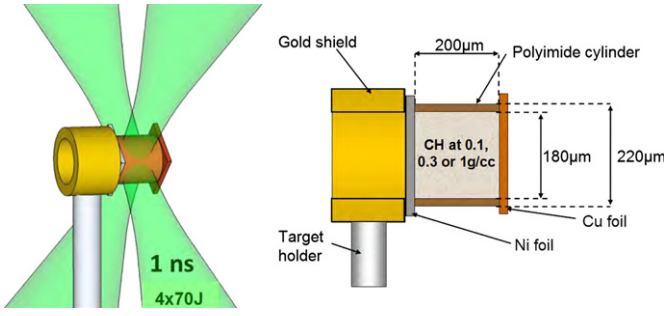

Fig. 1. Geometry of the compression with the four long pulse laser beams (left) and scheme of the cylindrical target (right).

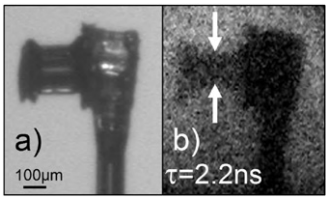

Fig. 2. Photography of the target before the shot (a) and X-ray radiography of the same target during the compression at $\tau=2.2$ ns (b).

the compression history of the target. To compare it with the 2D-hydrodynamic simulations from CHIC, we calculated Ti K_α X-ray transmission profiles through the 2D density maps given by the code. We assumed a laminar flux of the X-rays through the targets. Results are presented in Fig. 3.

The experimental points are corrected from the widening due to the resolution power of the imaging system: $FWHM_{corrected} = \sqrt{FWHM^2 - \Delta x^2}$. For each LP laser beam the simulations assumed a Gaussian-shaped spatial profile ($I_{laser} \sim e^{-(r/r_0)^2}$ with $r_0 = 80$ μm) and a 1 ns square temporal shape with a rising time of 200 ps. The computation has been realized for different laser energies, i.e., 4×70, 4×48 and 4×30 J, to take into account possible errors on the measurement of the experimental laser energy, energy losses in the focusing optics, the shape of focal spots and on the way the laser absorption is treated numerically by the code. The best agreement is found for 4×48 J. This fair agreement allows to be confident in the simulation results of the target's density and temperature during compression. Overall results of the hydrodynamic simulations for the different initial density targets are summarized in Table 1. They are compared to those obtained in planar compression geometry for 40 μm of Al [12].

The second phase was devoted to the study of the electron transport through the compressed targets. During this phase two Bragg spectrometers collected the Ni K_α and the Cu K_α emission at the rear side of the target. On one hand, because the electrons are generated at the front side of the Ni foil, the Ni $K_{\alpha(\beta)}$ emissions can be associated to the signature of the fast electron source. On the other hand, the Cu K_α, emitted either from the Cu-dopped foam or the rear side Cu foil, can be associated to the signature of the fast electrons crossing the target. The results of the HOPG spectrometer are shown in Fig. 4a. To account for the small shot-to-shot variations of the fast electrons source, the Cu K_α yields were adjusted to the Ni K_β yields for each shot. One can observe that the later the electrons are injected during the compression the less numerous they are to cross the target. The results from the Von-Hamos spectrometer confirm this trend. This behavior can be explained as follows: When the compression starts the mean foam density rises implying in the same way an average increase of the collisional processes (e.g. electron stopping power). The electrons are in this case slowed down more efficiently. Fig. 4b represents the diameter evolution of the rear side Cu K_α spot measured with the rear side imager. The results show that depending on ρ_0 or τ ($\tau < \tau_{stag}$ or $\tau > \tau_{stag}$, τ_{stag} being the stagnation time) the electrons can be either divergent (wide Cu K_α spot diameter) or collimated (small Cu K_α spot diameter).

Hybrid simulations of the electron transport have been performed in order to explain these trends. The description as well as the interpretation of the simulations will be the subject of an upcoming paper [13]. However, we can briefly explain the main results. Let us first assume that the fast electron beam is injected close to the beginning of the compression (i.e. $\tau < \tau_{stag}$). In this case, for both high and low ρ_0 targets, the plasma temperature is low and the converging compression shock front presents high resistivity gradients associated to high density gradients: $-\partial_r \eta \propto \partial_r n_e$, where η and n_e are, respectively, the resistivity and the electron density of the plasma. If the electrons are injected at this time they interact with these high resistivity gradients, inducing an azimuthal magnetic field B_φ, according to Faraday's law combined to Ohm's law: $\partial_t B_\varphi \sim -j_{hz} \partial_r \eta$ where j_{hz} is the electron current. This magnetic field acts as an electron collimator. Now let us suppose that the fast electron beam is injected later in time, i.e. $\tau > \tau_{stag}$. Although density and temperature are higher and more or less homogenized at the target interior, new resistivity gradients appear. Now this is

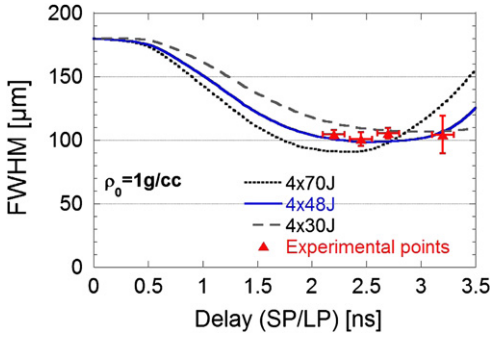

Fig. 3. Evolution the cylinder diameter as a function of the delay between SP and LP laser beams in the case of 1 g/cm^3 targets doped in mass with 30% of Cl. The experimental points are compared to simulations considering three different LP laser beam energies on target: 4×70, 4×48 and 4×30 J.

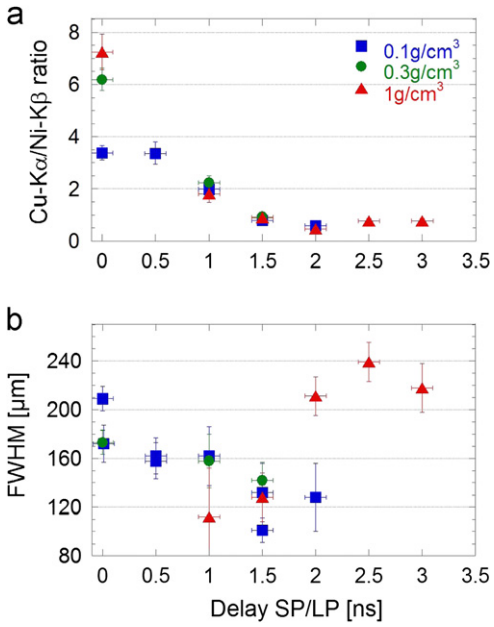

Fig. 4. Evolution of the fast electron fraction crossing the target at various times during the compression (top) and evolution of the rear side Cu K_α spot diameter (bottom) for the three different initial foam densities (0.1, 0.3 and 1 g/cm^3).

Table 1
Overall results from 2D CHIC simulations. τ_{stag} is the stagnation time (maximum compression), $\langle T \rangle_{stag}$ and $\langle \rho \rangle_{stag}$ are, respectively, the average temperature and density of the CH foam (for planar targets the average is taken on the total layer thickness), T_{max} and ρ_{max} correspond, respectively, to the maximum temperature and density achieved during the compression. Finally ϕ_{comp} represents the compression factor ($\phi_{comp} \equiv \rho_{max}/\rho_0$).

ρ_0 (g/cm^3)	τ_{stag} (ns)	$\langle T \rangle_{stag}$ (eV)	$\langle \rho \rangle_{stag}$ (g/cm^3)	T_{max} (eV)	ρ_{max} (g/cm^3)	ϕ_{comp}
0.1	1.9	100	4	140	5	50
0.3	2.15	45	3.8	85	5	16.7
1	2.5	15	3.2	42	13	13
2.7(Al)	–	4	5	–	6	2.2

mainly due to high temperature gradients located in the plasma surrounding the compressed core: $-\partial_r \eta \propto \partial_r T_e$. For low ρ_0 targets (0.1 or 0.3 g/cm^3), the fast electron beam interacts with these resistivity gradients since the latter are located close to the propagation axis. A collimating magnetic field is then induced. However for 1 g/cm^3 targets, the resistivity gradients are far from the propagation axis and do not interact with the fast electron beam. There is no collimating magnetic field generation, and consequently the electrons diverge across the target.

3. Planar compression experiment

3.1. Experimental setup

The experiment has been performed on the PICO2000 laser facility at LULI (France). Foil targets with variable Al *propagation* layer thickness (10, 20, 40 and 60 μm) were compressed at the rear side by a LP laser beam (4.5 ns,220 J at 2ω). An additional SP laser beam (1.5 ps,35 J at ω) was used to generate a fast electron current at the front side of the target. The estimated SP laser intensity on target was 1×10^{19} W cm^{-2}. In order to characterize the fast electron population during their transport, three thin layers of different K-shell fluorescent tracers, Ag (5 μm), Cu (10 μm) and Sn (10 μm), were embedded inside the target. The first one (Ag), used as a fast electron source tracer, was placed close to the front side of the target. The two other layers (Cu and Sn), used to characterize the fast electrons crossing the target, were situated after the Al propagation layer. A 14 μm polypropylene layer used as an ablator was positioned at the target rear side (see Fig. 5).

The chosen geometry of shock counter-propagative to the fast electron flux offers the advantage of creating homogeneous and controlled plasma conditions around the electron beam propagation axis. In this case the areal density (ρz) seen by the electrons during their propagation through the Al layer is kept constant as well as the collisional stopping power. We consider here two different experimental situations:

- In the first situation, to generate a fast electron beam propagating inside warm and dense Al we used along SP/LP delay. This delay was adjusted, according to CHIC hydrodynamic simulations and SOP (Streaked Optical Pyrometry) measurements, to fully compress the Al propagation layers but avoiding shock breakthrough at the target front side.
- In the second situation, still using both SP and LP laser beams but with a shorter delay, the electrons propagated in cold and solid Al. The delay was timed to avoid the shock reaching the Al propagation layer but enough long to create an ablation plasma at the target rear side working as a *get lost* layer for fast electrons and avoiding their refluxing in the K$_\alpha$ tracers.

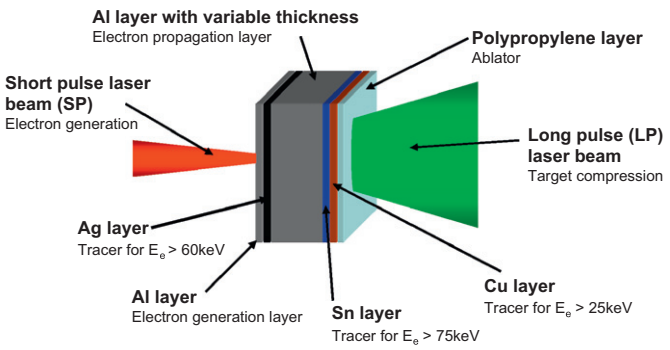

Fig. 5. Geometry of the compression and target details.

Several diagnostics were used to characterize the electron population. A spherical quartz crystal ($2d = 1.541$ Å, $R_c = 380$ mm) in Bragg incidence ($\theta_{Bragg} = 89.5°$) at ~ 210 mm from the target was used to image the rear side Cu K$_\alpha$ fluorescence on an Andor CCD camera placed ~ 2 m away. A Cauchois-type hard X-rays spectrometer [14] using a transmission curved quartz crystal ($2d = 0.6884$ nm) looked at the Sn and Ag K$_\alpha$ emissions from the target front side. A double channel HOPG crystals spectrometer ($2d = 0.6714$ nm) was also used to study the rear side emission from both Ag and Sn (first channel) and from Cu (second channel) layers.

3.2. Results and interpretation

With the help of the imager, the Cu K$_\alpha$ spot diameter was measured for different Al thicknesses in the case of compressed and non-compressed targets. The effects of the compression on the Al layer thickness seen by the electrons are taken into account. The results are plotted in Fig. 6 and can be associated to the electron beam radius evolution. From a geometrical point of view, it seems to be the same for both compressed and non-compressed targets. This is in agreement with previous measurements made in solid foil targets (e.g. Ref. [3]) but as the compression does not produce any effect on the fast electrons beam radius evolution, we deduce it is mainly a result of the fast electron generation process. The number of electrons can be estimated from the K$_\alpha$ fluorescence of each tracer layer thanks to the two spectrometers. The Sn K$_\alpha$ and the Cu K$_\alpha$ yields are the signature of the fast electrons (with energies > 75 and > 25 keV, respectively, according to the respective K-shell ionization cross-sections) reaching the target rear side. The Ag K$_\alpha$ yield is the signature of the fast electron source (with energies > 60 keV) generated at the target front side. In order to take into account shot-to-shot variations of the fast electron source the Sn K$_\alpha$ and the Cu K$_\alpha$ yields are adjusted to the Ag K$_\alpha$. The obtained ratios can thus be assimilated to the fraction of fast electron reaching the target rear side. The results are summarized in Fig. 7. According to preliminary hybrid simulations of the electron transport the resistive losses should be more important in compressed than in solid Al targets in relation to a resistivity increase from cold Al to warm Al ($T_e \sim T_F$). In Fig. 7a is presented the evolution of the Cu K$_\alpha$/ Ag K$_\alpha$ ratio as a function of the areal density ρz. The observed gap between compressed and solid cases is about $\sim 10\%$ for targets with Al layer thickness < 40 μm (i.e. $\rho z < 29$ mg/cm^2). Electrons with energy < 75 keV are thus more subject to resistive losses in compressed Al. Such behavior vanish for thicker Al layers where the integrated collisional losses erase any resistive effect. In Fig. 7b, the Sn K$_\alpha$/ Ag K$_\alpha$ ratio cannot be so well dissociated for compressed and non-compressed targets. In this case the electrons with energy > 75 keV seem to not be affected by the resistive mechanisms whatever the areal density. In our experimental conditions the

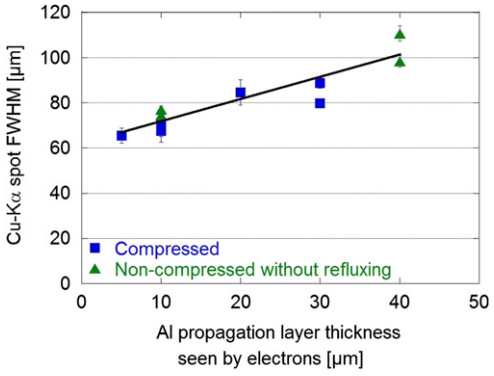

Fig. 6. Evolution of the rear side Cu K$_\alpha$ spot diameter against the Al propagation layer thickness seen by the electrons.

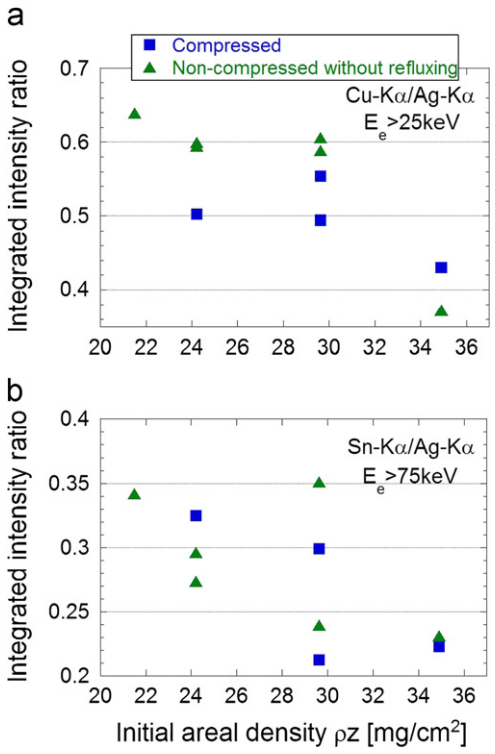

Fig. 7. Comparison of (a) the Cu K_α/ Ag K_α and (b) the Sn K_α/ Ag K_α ratios for the two different experimental situations.

electron beam current density has been estimated to 10^{11} A cm^{-2} at the source. This is in the range $10^{10} < j_h < 10^{12}$ A cm^{-2} where hybrid simulations predict a measurable stopping power change between solid and compressed Al, but the obtained results still demand verification by numerical simulations reproducing exactly our experimental conditions.

4. Conclusions

These two experiments performed in different compression geometries allowed us to study the fast electron transport in various kinds of plasmas. In the case of the cylindrical compression, we demonstrate the possibility to infer plasma characteristics with the help of X-ray and proton radiographies coupled to hydrodynamic simulations. Thus, the measured densities and temperatures ranged from 2 to 13 g/cm^3 and 30 to 120 eV, respectively, equivalent to the dense plasmas found in the HiPER baseline target at stagnation [7] located $\sim$70 μm from the compressed D–T shell. Such geometry has the advantage, for certain experimental conditions, to induce high radial resistivity gradients leading to the collimation of fast electrons. Planar compression geometry produces lower compression factors but the simpler approach allows to isolate and estimate the importance of particular aspects of the fast electron transport, e.g. the resistive stopping power associated to the self-generated fields. In our experimental conditions, we infer that only electrons of energy <75 keV are more affected by the resistive losses. Besides, from the size of the Cu K_α signals, we deduced that the compression does not produce any change on the fast electron beam propagation geometry, being mainly a product of the fast electron generation.

References

[1] M. Tabak, et al., Phys. Plasmas 1 (5) (1994) 1626.
[2] M.H. Key, et al., Phys. Plasmas 5 (1998) 1966.
[3] J.J. Santos, et al., Phys. Rev. Lett. 89 (2002) 025001.
[4] J.S. Green, et al., Phys. Rev. Lett. 100 (2008) 015003.
[5] F.N. Beg, et al., Phys. Plasmas 4 (2) (1997) 447.
[6] F. Perez, et al., Plasma Phys. Controlled Fusion 51 (2009) 124035.
[7] X. Ribeyre, et al., Plasma Phys. Controlled Fusion 50 (2008) 025007.
[8] P.H. Maire, et al., SIAM J. Sci. Comput. 29 (4) (2007) 1781.
[9] Y. Agliskiy, et al., Appl. Opt. 37 (22) (1998) 5253.
[10] M. Borghesi, et al., Phys. Plasmas 9 (5) (2002) 2214.
[11] L. Volpe, et al., Nucl. Instr. and Meth. A, this issue.
[12] J.J. Santos, et al., Plasma Phys. Controlled Fusion 51 (2009) 014005.
[13] F. Perez, et al., in preparation.
[14] J.F. Seely, et al., Appl. Opt. 47 (15) (2008) 2767.